Estimation of the 3D correlation structure of an alluvial aquifer from surface-based multi-frequency GPR reflection data

Zhiwei Xu[1, 2], James Irving[2,*], Kyle Lindsay[3], John Bradford[4], Peimin Zhu[1], and Klaus Holliger[2, 5]

1. Institute of Geophysics and Geomatics, China University of Geosciences, Wuhan, China
2. Institute of Earth Sciences, University of Lausanne, Lausanne, Switzerland
3. Department of Geosciences, Boise State University, Boise, USA
4. Geophysics Department, Colorado School of Mines, Golden, USA
5. School of Earth Sciences, Zhejiang University, Hangzhou, China

* Corresponding author: james.irving@unil.ch

Abstract

Knowledge about the stochastic nature of heterogeneity in subsurface hydraulic properties is critical for aquifer characterization and the corresponding prediction of groundwater flow and contaminant transport. Whereas the vertical correlation structure of the heterogeneity is often well constrained by borehole information, the lateral correlation structure is generally unknown because the spacing between boreholes is too large to allow for its meaningful inference. There is, however, evidence to suggest that information on the lateral correlation structure may be extracted from the correlation statistics of the subsurface reflectivity structure imaged by surface-based ground-penetrating radar (GPR) measurements. To date, case studies involving this approach have been limited to 2D profiles acquired at a single antenna center frequency in areas with limited complementary information. As a result, the practical reliability of this methodology has been difficult to assess. Here, we extend previous work to 3D and consider reflection GPR data acquired using two antenna center frequencies at the extensively explored and well constrained Boise Hydrogeophysical Research Site (BHRS). We find that the results obtained using the two GPR frequencies are consistent with each other, as well as with information from a number of other studies at the BHRS. In addition, contrary to previous 2D work, our results indicate that the surface-based reflection GPR data are not only sensitive to the aspect ratio of the underlying heterogeneity, but also, albeit to a lesser extent, to the so-called Hurst number, which is a key parameter characterizing the local variability of the fine-scale structure.

Keywords: lateral correlation structure, aquifer heterogeneity, Monte-Carlo inversion, aspect ratio, Hurst number, water content, ground-penetrating radar

1. Introduction

An important objective in many hydrogeological studies is the characterization of subsurface heterogeneity within an aquifer for the subsequent prediction of groundwater flow and contaminant transport (e.g., Sudicky, 1986; Mas - Pla et al., 1992; Phanikumar et al., 2005; Salamon et al., 2007; Hu et al., 2009; Radu et al., 2011). Typical hydrogeological characterization methods have significant limitations in this regard, as there exists a wide gap in terms of spatial coverage and resolution between local borehole-based studies and larger-scale aquifer tests (e.g., Sudicky, 1986; Kobr et al., 2005; Leven and Dietrich, 2006). This gap can at least be partially bridged through specifically targeted geophysical measurements (e.g., Rubin and Hubbard, 2006; Hubbard and Linde, 2010). In this regard, recent evidence suggests that high-resolution surface-based reflection ground-penetrating radar (GPR) data may offer important information on subsurface geostatistical properties (e.g., Rea and Knight, 1998; Gloaguen et al., 2001; Tronicke et al., 2002; Kowalsky et al., 2005; Rubin and Hubbard, 2006). This comes as a result of the close relationship that exists between soil water content and the high-frequency electromagnetic wave velocity (e.g., Greaves et al., 1996; Van Overmeeren et al., 1997; Al Hagrey and Müller, 2000).

Whereas the vertical correlation structure of subsurface heterogeneity within an aquifer is often well constrained by borehole information (e.g., Ritzi et al., 1994), the lateral correlation structure tends to be largely unknown because the boreholes are generally too sparse for its reliable inference. To date, several attempts have been made to relate the lateral correlation statistics of surface-based reflection GPR data to those of the investigated subsurface region (e.g., Rea and Knight, 1998; Oldenborger et al., 2004; Knight et al., 2004, 2007; Dafflon et al., 2005; Irving and Holliger, 2010; Irving et al., 2009, 2010). Rea and Knight (1998) compared the correlation structure of an outcrop image with that of the corresponding GPR data and found good overall agreement. Oldenborger et al. (2004) demonstrated that the geostatistical characteristics of GPR reflection data are quite robust to the effects of data processing including gain functions and migration, but noted that they will not be identical to those of the underlying porosity distribution because they are strongly influenced by the choice of the antenna frequency. Dafflon et al. (2005) complemented and extended the work of Rea and Knight (1998) and considered a realistic and highly versatile autocorrelation model to describe the subsurface heterogeneity. Knight et al. (2007) observed similarities between the horizontal correlation statistics of GPR reflection data and those of closely spaced neutron-probe water-content measurements, but pointed to the results of previous work demonstrating that the lateral correlation structure of a GPR reflection image will be strongly influenced by the vertical measurement resolution, which in turn is controlled by the antenna center frequency (Knight et al., 2004).

Irving et al. (2009) were the first to present a physically and mathematically consistent model relating the 2D spatial autocorrelation of the subsurface water-content distribution to that of the corresponding GPR data, taking into account the effects of antenna frequency. Based on this model, they proposed a Bayesian Markov-chain-Monte-Carlo (MCMC) inversion approach to estimate the subsurface horizontal correlation statistics from the GPR reflection data. They found that unique recovery of the lateral correlation structure is dependent upon accurate knowledge of the vertical correlation structure. This finding was subsequently demonstrated mathematically by Irving and Holliger (2010). This inversion methodology was successfully applied to both synthetic and field GPR measurements, as well as to synthetic seismic reflection data (Irving et al., 2010; Scholer et al., 2010). However, all work so far has been limited to 2D profiles acquired at a single source frequency in areas where limited complementary information has been available. As a result, the practical reliability of this approach remains difficult to assess.

In this paper, we seek to address the above limitations by extending the approach of Irving et al. (2009) from 2D to 3D and by considering a pertinent case study involving the use of multiple GPR antenna center frequencies at a well characterized hydrogeophysical test site. We begin by describing the relationship between the 3D spatial autocorrelation of the high-frequency subsurface electromagnetic wave velocity distribution and that of the corresponding depth-migrated GPR reflection image. Next, we outline how we estimate the parameters describing the considered subsurface autocorrelation model from the GPR data using a Monte-Carlo inversion strategy. Finally, we demonstrate the successful application of this methodology to 3D GPR field data acquired using 100-MHz and 200-MHz antennas at the Boise Hydrogeophysical Research Site (BHRS), Idaho, USA.

2. Methodology

2.1. Von Kármán autocorrelation function

Seismic and radar wave velocity heterogeneities in the subsurface are commonly characterized as a superposition of a slowly varying or constant deterministic background velocity model and a stochastic velocity perturbation field (e.g., Gibson, 1991; Holliger et al., 1992). Following this assumption, the 3D subsurface high-frequency electromagnetic velocity field can be written as

$$\mathrm{v}(\mathrm{x},\mathrm{y},\mathrm{z}) = \mathrm{v}_0(\mathrm{x},\mathrm{y},\mathrm{z}) + \Delta\mathrm{v}(\mathrm{x},\mathrm{y},\mathrm{z}), \tag{1}$$

where $\mathrm{v}_0(\mathrm{x},\mathrm{y},\mathrm{z})$ is the background velocity field and $\Delta\mathrm{v}(\mathrm{x},\mathrm{y},\mathrm{z})$ represents the stochastic perturbation, the latter of which we assume to be zero-mean and, to a first approximation, multi-Gaussian distributed (e.g., Holliger, 1996) and whose parametric spatial correlation properties we wish to estimate. To this end, we consider the von Kármán spatial autocorrelation function, which has been widely used to describe subsurface spatial variability in both borehole data analysis (e.g., Dolan and Bean, 1997; Jones and Holliger, 1997) and numerical simulations of wave-propagation phenomena (e.g., Frankel and Clayton, 1986; Hartzell et al., 2010). The 3D form of the von Kármán autocorrelation equation for anisotropic velocity heterogeneity aligned along arbitrary orthogonal coordinate axes x', y', and z' can be written as (e.g., Goff and Jordan, 1988)

$$\mathrm{R}_{\mathrm{vv}}(\delta\mathrm{x}',\delta\mathrm{y}',\delta\mathrm{z}') = \frac{\mathrm{r}^{\nu}\mathrm{K}_{\nu}(\mathrm{r})}{2^{\nu-1}\mathrm{K}_{\nu}\Gamma_{\nu}(0)} \tag{2}$$

where $\delta\mathrm{x}'$, $\delta\mathrm{y}'$, $\delta\mathrm{z}'$ are the spatial autocorrelation lags in the x'-, y'-, and z'-directions, respectively, $\mathrm{K}_{\nu}(r)$ is the modified Bessel function of the second kind of order $0 \leq \nu \leq 1$, Γ is the gamma function, and

$$r = \sqrt{\left(\frac{\delta x'}{a_{x'}}\right)^2 + \left(\frac{\delta y'}{a_{y'}}\right)^2 + \left(\frac{\delta z'}{a_{z'}}\right)^2} \tag{3}$$

is a normalized lag parameter with $a_{x'}$, $a_{y'}$, and $a_{z'}$ denoting the spatial correlation lengths along x', y', and z', respectively. Eq. (2) defines an anisotropic heterogeneous medium showing self-similar or fractal behavior at scales shorter than the correlation lengths. The parameter ν, which is generally referred to as the Hurst number, determines the decay rate of the autocorrelation function at near-zero lag values and, as such, characterizes the local variability of the considered stochastic medium. Values of ν close to zero and one are indicative of locally highly variable and locally very smooth media, respectively. A ν-value of 0.5, on the other hand, corresponds to a so-called Brownian stochastic process described by the well-known exponential autocorrelation function.

In general, x', y', and z' in Eqs. (2) and (3), which correspond to the principal axes of anisotropy of the subsurface velocity heterogeneity, will not be aligned with the local x, y, and z coordinate axes that typically reflect the GPR data acquisition geometry. In other words, it is rarely the case that the ellipsoid describing the velocity heterogeneity will have principal axes that are consistent with the 3D GPR data set upon which the local coordinate axes are typically defined. As a result, an orthogonal transformation is needed to use Eqs. (2) and (3) in the local x, y, and z coordinate system. This transformation is described by

$$\begin{bmatrix} x' \\ y' \\ z' \end{bmatrix} = \begin{bmatrix} | & | & | \\ \mathbf{T}_1 & \mathbf{T}_2 & \mathbf{T}_3 \\ | & | & | \end{bmatrix} \begin{bmatrix} x \\ y \\ z \end{bmatrix}, \tag{4}$$

where the columns $\mathbf{T}_i$ of orthogonal transformation matrix $\mathbf{T}$ are obtained by expressing unit vectors in the x-, y-, and z-directions in terms of the coordinates x', y', and z' (e.g., Roman et al., 2005). To estimate the directions of predominant velocity anisotropy in our work, which are required for the inversion procedure described in Section 2.3, we use the dominant dip angles observed in the reflection GPR data as well as the corresponding 3D data autocorrelation. More details on how this is done are given in Section 3.2 when we apply our approach to the BHRS field data sets.

2.2. Forward model

To relate the stochastic properties of a depth-migrated 3D GPR reflection image to those of the underlying high-frequency electromagnetic wave velocity distribution, we extend the method of Irving et al. (2009) from 2D to 3D. To this end, we consider a modified version of the primary reflectivity section (PRS) model (e.g., Gibson, 1991; Pullammanappallil et al., 1997), where the 3D GPR image, $d(x, y, z)$, can be expressed as the convolution of a source wavelet, $w(z)$, the subsurface reflectivity coefficient field, $r(x, y, z)$, and a 2D horizontal-resolution filter, $h(x, y)$. As the distribution of reflection coefficients in the subsurface can be approximated by the vertical spatial derivative of the velocity field, $v(x, y, z)$, this leads to

$$\begin{aligned} d(x,y,z) &\approx w(z) * r(x,y,z) * h(x,y) \\ &\approx w(z) * \frac{\partial}{\partial z} v(x,y,z) * h(x,y), \end{aligned} \tag{5}$$

where the asterisk denotes the convolution operator. It is important to note that the modified PRS model described by Eq. (5) assumes that: (i) single scattering predominates, which is a basic assumption inherent to most seismic and GPR processing, imaging, and interpretation strategies (e.g., Aki and Chouet, 1975; Sato, 1977); (ii) dispersion in the GPR data can be ignored such that a constant wavelet shape can be approximately assumed; and (iii) the data have been properly depth-migrated. Under these conditions, Eq. (5) will capture the essential features of a 3D GPR reflection image.

The operator $\mathrm{h(x,y)}$ in Eq. (5) is required to account for the limited lateral resolution of a migrated reflection image (e.g., Berkhout, 1984). Following Irving et al. (2009), we use a Gaussian low-pass filter for this purpose

$$\mathrm{h(x,y)} = \exp\left(-\frac{x^2+y^2}{2c^2}\right), \tag{6}$$

where c determines the filter width and is set such that the diameter of the filter function where h reaches 1% of its maximum value is equal to the dominant wavelength of the GPR pulse.

Noting that the vertical derivative operator in Eq. (5) can be treated as a filter whose position in the equation can be shifted to act on the wavelet, we can write the equation as

$$\mathrm{d(x,y,z)} \approx \mathrm{v(x,y,z)} * \mathrm{f(x,y,z)}, \tag{7}$$

where

$$\mathrm{f(x,y,z)} \approx \frac{\partial}{\partial \mathrm{z}} \mathrm{w(z)} * \mathrm{h(x,y)}. \tag{8}$$

Transforming Eq. (7) into the frequency domain and taking the squared magnitude of both sides, we obtain a relationship between the 3D power spectra of all quantities

$$\left|D(k_x,k_y,k_z)\right|^2 \approx \left|V(k_x,k_y,k_z)\right|^2 \cdot \left|F(k_x,k_y,k_z)\right|^2, \tag{9}$$

where k_x, k_y, and k_z are the spatial wavenumbers in the x-, y-, and z- directions, respectively. Taking the inverse Fourier transform and making use of the Wiener-Khintchine theorem linking the power spectra with the autocorrelation functions then yields

$$R_{dd}(\delta x, \delta y, \delta z) \approx R_{vv}(\delta x, \delta y, \delta z) * R_{ff}(\delta x, \delta y, \delta z), \tag{10}$$

where δx, δy, and δz denote the spatial autocorrelation lags along x, y, and z.

Eq. (10) states that the 3D spatial autocorrelation of a depth-migrated GPR reflection image, $R_{dd}(\delta x, \delta y, \delta z)$, will be approximately equal to the 3D convolution of the autocorrelation of the underlying subsurface velocity field, $R_{vv}(\delta x, \delta y, \delta z)$, and that of the filtered source wavelet, $R_{ff}(\delta x, \delta y, \delta z)$. This means that, with knowledge of $R_{ff}(\delta x, \delta y, \delta z)$, we can estimate the parameters of the von Kármán autocorrelation function describing $R_{vv}(\delta x, \delta y, \delta z)$ given $R_{dd}(\delta x, \delta y, \delta z)$. Similar to our previous work involving 2D data (Irving et al., 2009, 2010), we can obtain the autocorrelation of $w(z)$ from $R_{dd}(0,0,\delta z)$, which is the average vertical autocorrelation of the migrated GPR image. Thus, $R_{ff}(\delta x, \delta y, \delta z)$ can be calculated through 3D convolution of $R_{dd}(0,0,\delta z)$ with the autocorrelation of the horizontal-resolution filter, $h(x,y)$, and that of a finite-difference vertical derivative operator.

2.3. Inversion strategy

Given knowledge of $R_{ff}(\delta x, \delta y, \delta z)$ and $R_{dd}(\delta x, \delta y, \delta z)$, which are both computed from the 3D GPR image, we wish to estimate the parameters governing

$R_{vv}(\delta x, \delta y, \delta z)$ using the forward model given in Eq. (10). Specifically, our aim is to recover information on the correlation lengths, $a_{x'}$, $a_{y'}$, $a_{z'}$ as well as on the Hurst number ν, which together parameterize the velocity heterogeneity described by the von Kármán autocorrelation model through Eqs. (2) and (3). As this represents a low-dimensional but strongly non-linear inverse problem, we employ a brute-force Monte-Carlo approach, which is consistent with the work of Irving et al. (2010) and Scholer et al. (2010). Although the original Bayesian MCMC inversion methodology presented by Irving et al. (2009) allows, in theory, for the quantification of posterior uncertainties of the estimated model parameters, it relies upon accurate statistical characterization of the residuals between the observed GPR image autocorrelation and that calculated using Eq. (10), which in general are not well known. A Monte-Carlo approach avoids these limitations and allows for great flexibility with regard to the criteria upon which parameter sets are accepted, albeit with the caveat that the corresponding inversion results do not represent samples from a Bayesian posterior distribution.

To carry out an inversion using Eq. (10), we require a metric of acceptable fit between the predicted autocorrelation of a 3D GPR image based on a particular test set of von Kármán parameters, which we denote as $R_{dd}^{pred}(\delta x, \delta y, \delta z)$, and the observed GPR image autocorrelation, which we denote using $R_{dd}^{obs}(\delta x, \delta y, \delta z)$. In previous 2D work, Irving et al. (2009, 2010) and Scholer et al. (2010) found that considering only the fit in the lateral direction was sufficient for this purpose, as the vertical correlation structure of a GPR reflection image is largely controlled by the source pulse. Similarly, for our 3D investigation, we have found that if the fit to the observed autocorrelation data in the $\delta z = 0$ plane (i.e., $R_{dd}^{obs}(\delta x, \delta y, 0)$) is adequate, then, in general, we will have an adequate fit to the entire 3D GPR image autocorrelation. We therefore prescribe fitting bounds around $R_{dd}^{obs}(\delta x, \delta y, 0)$ within which acceptable lateral autocorrelation data predicted using Eq. (10) (i.e., $R_{dd}^{pred}(\delta x, \delta y, 0)$) must lie (e.g., Irving et al., 2010; Scholer et al., 2010). In this regard, we define the maximum absolute fitting error

$$\xi = \max\left\{\left|R_{dd}^{pred}(\delta x, \delta y, 0) - R_{dd}^{obs}(\delta x, \delta y, 0)\right|\right\}, \tag{11}$$

where R_{dd}^{pred} and R_{dd}^{obs} are considered to be normalized to a maximum value of one. Test sets of von Kármán model parameters that are deemed acceptable in the inversion procedure must have a ξ-value less than or equal to some user-prescribed threshold. In this way, our inversion approach is similar to the generalized likelihood uncertainty estimation (GLUE) technique (Beven and Binley, 1992), whereby "behavioral" sets of model parameters are identified within a Monte-Carlo framework based on whether the corresponding predicted data fall within specified bounds.

Our Monte-Carlo inversion strategy for estimating $a_{x'}$, $a_{y'}$, $a_{z'}$ and ν from the observed 3D GPR image autocorrelation is summarized by the following steps:

1. Select the appropriate region of the depth-migrated 3D GPR image for analysis, and estimate the principal axes of the ellipsoid describing the subsurface velocity heterogeneity, x', y', and z'. More details on how this is accomplished are provided in Section 3.2.
2. Calculate the observed 3D autocorrelation of the GPR reflection image,

$R_{dd}^{obs}(\delta x, \delta y, \delta z)$, and use the vertical component, $R_{dd}^{obs}(0,0,\delta z)$, to compute $R_{ff}(\delta x, \delta y, \delta z)$ by convolving it with the autocorrelation of $h(x, y)$ in Eq. (6) and that of a finite-difference vertical derivative operator.

3. Define uniform prior ranges for the von Kármán model parameters describing the velocity heterogeneity, $a_{x'}$, $a_{y'}$, $a_{z'}$ and ν.
4. Choose a maximum permissible value, ξ^*, for the fitting error given by Eq. (11). This defines what we deem to be an acceptable fit between the predicted and observed 3D GPR image autocorrelations.
5. Randomly draw a proposed set of values for $a_{x'}$, $a_{y'}$, $a_{z'}$ and ν from the prior distributions defined in Step 3 and compute $R_{vv}(\delta x, \delta y, \delta z)$ using Eqs. (2) and (3).
6. Calculate the corresponding predicted GPR image autocorrelation, $R_{dd}^{pred}(\delta x, \delta y, \delta z)$, using Eq. (10) with $R_{vv}(\delta x, \delta y, \delta z)$ from Step 5 and $R_{ff}(\delta x, \delta y, \delta z)$ from Step 2.
7. Calculate ξ using Eq. (11). If $\xi < \xi^*$, then the proposed set of von Kármán model parameters is accepted. Otherwise, it is rejected.
8. Return to Step 5 and repeat until the desired number of accepted sets of von Kármán model parameters has been obtained.

It is important to note that since each accepted set of von Kármán model parameters is generated independently with our methodology (i.e., not depending on the previous parameter set values), a parallel computational strategy can be adapted in order to generate stochastic realizations more efficiently. That is, Steps 5 to 8 in our inversion workflow can be assigned to different processors on a cluster-type computer. Compared to the MCMC inversion approach of Irving et al. (2009), this is a notable advantage.

3. Application to field data

3.1. Site description

We now show the application of the previously described 3D inversion methodology to field GPR reflection data acquired at the BHRS using two different antenna center frequencies. The BHRS is a research site located on a gravel bar adjacent to the Boise River, ~15 km from downtown Boise, Idaho, USA (Figure 1a). It contains 13 boreholes in a central area, which has a diameter of ~20 m, and five boreholes near its borders located at distances of ~10 to 35 m from this central area. The underlying braided-river aquifer consists of late Quaternary fluvial deposits dominated by coarse cobbles and sand. These are followed by a layer of red clay, which is situated at ~20-m depth. Over the past two decades, the site has been extensively used for the testing, validation, and improvement of a wide variety of geophysical and hydrogeological methods for characterizing heterogeneous aquifers (e.g., Tronicke et al., 2004; Bradford et al., 2009; Nichols et al., 2010; Dafflon et al., 2011; Dafflon and Barrash, 2012; Cardiff et al., 2013; Hochstetler et al., 2016).

3.2. Database

The 3D GPR reflection data considered in our study were acquired during the summer of 1998 using a PulseEkko Pro 100 system (Sensors & Software Inc.) with nominal antenna center frequencies of 100 and 200 MHz. The 100- and 200-MHz data were collected in common-offset mode using transmitter-receiver antenna spacings of 1 m and 0.5 m, respectively. The GPR survey grid had dimensions of 30 m in the in-line (x) direction and 18 m in the cross-line (y) direction (Figure 1b). Traces were recorded every 0.1 m along each survey line, with a line spacing of 0.2 m. A time sampling interval of 0.8 ns was used and recordings were made over 400 ns. Note that the corresponding Nyquist frequency of 625 MHz is well beyond the maximum emitted frequency of the 200-MHz antennas, which is believed to be no greater than 450 MHz. For each recorded trace, 32 stacks were performed in order to improve the signal-to-noise ratio of the data.

Processing of the GPR data consisted of band-pass filtering between 25 MHz and 450 MHz, automatic gain control (AGC) with a large time window of 50 ns, and constant-velocity 3D migration (e.g., Stolt, 1978) using a velocity of 0.08 m/ns determined from the analysis of common-mid-point measurements. In the resulting GPR images, the depth sampling interval is 0.037 m. Although, in theory, a spatially variable velocity field is required to obtain the most accurate subsurface image through migration, extensive testing on synthetic data has indicated that constant-velocity migration with the average prevailing velocity is perfectly adequate for the kind of stochastic analysis considered in this paper, most notably in the presence of velocity heterogeneities comparable to those observed at the BHRS (e.g., Irving et al., 2009; Bradford et al., 2009; Irving et al., 2010). In addition, Oldenborger et al. (2004) found that the spatial autocorrelation of a reflection GPR image is relatively insensitive to the details of the data processing and migration.

Figures 2a and 2b show the processed 100- and 200-MHz GPR images from 0- to 10-m depth, respectively. The horizontal reflector at ~2.5 m depth is the water table. Note that similarities can be seen in the two images in terms of the response to dominant reflecting interfaces in the subsurface. However, the 200-MHz data appear to be laterally more heterogeneous than their 100-MHz counterparts. The main reason for this phenomenon is that non-specular reflectors, which may effectively “line up” laterally when imaged using lower-frequency antennas, can become discontinuous when imaged using higher-frequency antennas (Irving et al., 2009; Scholer et al., 2010).

To estimate the principal axes of the ellipsoid describing the subsurface velocity heterogeneity at the BHRS, we consider the higher-resolution 200-MHz measurements, but comparable results are obtained for the 100 MHz data. Careful analysis of the data in Figure 2b indicates that the dominant dip of the sediments is roughly 8 degrees with respect to the horizontal. Taking the cross product of the vectors representing the intersection of this dipping plane with the x=0 and y=0 planes yields one of the principal axes of the heterogeneity, which is perpendicular to the predominant dip of the sedimentary layering. Next, we calculate the 3D autocorrelation of the GPR image (Figure 3a). Examination of this autocorrelation through the origin along the previously calculated dipping plane yields an ellipse whose major axis corresponds to another one of the principal directions (Figure 3b). Finally, the third principal direction is found by taking the cross product of the two previously determined ones, making sure that the resulting vector forms a right-handed coordinate system with the others. This direction corresponds to the minor axis of the ellipse along the dipping plane (Figure 3c). For the BHRS data, the above analysis yielded the following unit vectors $\hat{\mathbf{x}}'$, $\hat{\mathbf{y}}'$, and $\hat{\mathbf{z}}'$ along the x'-, y'-, and z'-directions, respectively:

$$\hat{\mathbf{x}}' = \begin{bmatrix} 0.9612 \\ 0.2452 \\ -0.1264 \end{bmatrix}, \quad \hat{\mathbf{y}}' = \begin{bmatrix} -0.2530 \\ 0.9662 \\ -0.0496 \end{bmatrix}, \quad \hat{\mathbf{z}}' = \begin{bmatrix} 0.1100 \\ 0.0797 \\ 0.9907 \end{bmatrix}. \tag{11}$$

We see that these vectors are close, but not identical, to those defining a standard Cartesian coordinate system aligned with the GPR survey grid.

3.3. Inversion procedure

For all of the inversion results presented in this paper, we consider a maximum fitting-error of $\xi^* = 0.12$. This means that all sets of von Kármán parameters whose corresponding predicted GPR image autocorrelations were within a distance of 0.12 from the observed autocorrelation in the $\delta z = 0$ plane were accepted in the Monte-Carlo inversion procedure. This choice, which is admittedly subjective and based on what we view to represent a “behavioral” set of model parameters in terms of bounding the observations (Beven and Binley, 1992), is more visually intuitive and less problematic than other fitting metrics based upon assumed knowledge regarding the statistical distribution of the data residuals (e.g., Irving et al., 2009). In this context, it is again important to note that our inversion results cannot be regarded as samples from a formal Bayesian posterior distribution.

For the inversions, we considered the 100- and 200-MHz GPR data over a restricted depth range from 2.5 m to 8 m. The upper limit of this range corresponds to the position of the water table at the time the measurements were taken, whereas the lower limit represents the maximum depth of penetration of the 200-MHz data. In this way, the estimated geostatistics of the high-frequency electromagnetic wave velocity at the BHRS correspond to saturated fluvial sediments. Given the quasi-linear relationship between water content and velocity over a limited range (e.g., Irving et al., 2009), the corresponding results can therefore be interpreted in terms of porosity. In this regard, the prior range of acceptable values for the vertical correlation length $a_{z'}$ was set between 0.1 and 2 m. This range was constrained by previous analyses of porosity log data along BHRS boreholes C5 and C6 assuming the same parametric autocorrelation model as the one used in this study (Dafflon et al., 2009). Similarly, based on a comprehensive review of the fractal nature of rock physical properties in sedimentary rocks (Hardy and Beier, 1994), the prior range for the Hurst number ν was set between 0.1 and 0.5. Based on the available evidence, ν-values larger than 0.5 are extremely unlikely in general (Hardy and Beier, 1994) and particularly within the given context (e.g., Dafflon et al., 2009). Conversely, ν-values close to zero are realistic, but would render evaluation of the parametric autocorrelation function given by equation (2) error-prone due to the singularity of the associated Bessel function. The prior ranges for the horizontal correlation lengths $a_{x'}$ and $a_{y'}$, on the other hand, which cannot be reliably constrained by borehole measurements, were both set rather broadly between 0.1 and 20 m.

For each GPR data set, the previously described Monte-Carlo inversion procedure was run until 2000 accepted sets of von Kármán autocorrelation model parameters were obtained. Similar to previous work with 2D data (e.g., Irving et al., 2009, 2010; Irving and Holliger, 2010), the 3D inversion cannot constrain uniquely the horizontal correlation lengths, but rather only the horizontal-to-vertical aspect ratios of the underlying heterogeneity. As a result, we present our results in terms of the aspect ratios $a_{x'}/a_{z'}$ and $a_{y'}/a_{z'}$, along with the lateral aspect ratio $a_{y'}/a_{x'}$.

3.4. Results

Figures 4 and 5 present histograms of $a_{x'}/a_{z'}$, $a_{y'}/a_{z'}$, $a_{y'}/a_{x'}$, and ν, which were obtained from the 100- and 200-MHz BHRS inversion results, respectively. The corresponding summary statistics are provided in Table 1. We see that our Monte-Carlo inversion procedure has resulted in generally well-defined, quasi-normal distributions for the three considered aspect ratios. The mean values for the horizontal-to-vertical aspect ratio in x'-direction, $a_{x'}/a_{z'}$, are 6.3 and 5.7 for the 100- and 200-MHz data, respectively, which are consistent (Figures 4a and 5a). The estimates of 13.1 and 10.2 for the horizontal-to-vertical aspect ratio in y' direction, $a_{y'}/a_{z'}$, differ more significantly between the 100- and 200-MHz data (Figures 4b and 5b), but are still in good agreement given the corresponding standard deviations (Table 1). All of these values correspond well with values inferred by Dafflon et al. (2009) from the analysis of porosity log data along boreholes C5 and C6, which are aligned at an oblique angle to our y'-direction, and corresponding crosshole tomographic GPR measurements. In that paper, a range of horizontal-to-vertical aspect ratios between 6 and 20 was considered to generate conditional stochastic realizations of porosity. The authors found that intermediate values in this range exhibited the best qualitative agreement with the corresponding full-waveform crosshole tomographic GPR image of Ernst et al. (2007), which is expected to have a resolution in the decimeter range.

Our inferred values for $a_{x'}/a_{z'}$ and $a_{y'}/a_{z'}$ complement the work of Dafflon and Barrash (2012), who performed 3D stochastic simulations of the porosity structure of the BHRS constrained by all available porosity logs and crosshole GPR tomograms. The simulations were based on an exponential autocorrelation model, which was assumed to be laterally isotropic, i.e., $a_{x'} = a_{y'}$. Both the vertical and the lateral correlation lengths were estimated based on the analysis of the porosity logs. As pointed out earlier, and indeed confirmed by Dafflon and Barrash (2012), the comparatively large spacings between the individual boreholes make this approach inherently prone to significant uncertainties with regard to the estimation of the lateral correlation lengths. This, in turn, finds its expression in a relatively wide range of horizontal-to-vertical aspect ratios between 3 and 6 estimated by Dafflon and Barrash (2012), which is biased towards too low values compared the results of Dafflon et al. (2009) and Ernst et al. (2007). The upper end of this range, which is preferred by Dafflon and Barrash (2012) is broadly compatible with our estimates.

Regarding the horizontal aspect ratio $a_{y'}/a_{x'}$, which describes the degree of anisotropy in the velocity heterogeneity in the x'-y' plane, the mean inferred values from our analysis are 2.1 and 1.8 for the 100- and 200-MHz data, respectively (Figures 4c and 5c). These values are consistent with the overall structure of the braided-stream deposits at the BHRS, for which the correlation length in the flow direction of the Boise River along the y'-axis is known to be larger than that in the perpendicular direction. Indeed, core studies by Reboulet and Barrash (2003) from boreholes B1, B2, and C2, which are along the y-direction (Figure 1), revealed the presence of a larger sand channel at 6 to 7 m depth, whereas Bradford et al. (2009) found several smaller-scale channels or lenses in the x-direction through porosity log analyses.

In contrast to previous work of Scholer et al. (2010), our results suggest that the considered 3D GPR reflection data also exhibit some sensitivity to the Hurst number ν, which, as outlined earlier, characterizes the local variability of the velocity heterogeneity (Figures 4d and 5d). As the corresponding histograms are distinctly asymmetric and dispersed, we consider the peak values of the distributions, which are 0.12 and 0.18 for the 100- and 200-MHz data, respectively. Not only are these values reasonably consistent with one another, they are also in agreement with the value of 0.2 inferred by Dafflon et al. (2009) from porosity log measurements along boreholes C5 and C6, as well as the seemingly universal observation that the Hurst numbers of most rock physical properties in sedimentary environments are characterized by very small ν-values regardless of the geological setting (e.g., Hardy and Beier, 1994).

Finally, one item of particular interest, which is somewhat counter-intuitive, is the increased standard deviation of the estimated aspect ratios for the 200-MHz data as compared to those for 100-MHz data (Table 1). While this phenomenon is not fully understood and remains a topic of current work, it is consistent with corresponding observations made by Scholer et al. (2010) for synthetic reflection seismic data simulated at different dominant source frequencies.

4. Conclusions

The main objective of this study was to implement and validate a methodology for estimating the lateral correlation structure of an alluvial aquifer from surface-based 3D GPR reflection data. To this end, we have developed a relationship between the autocorrelation of the 3D GPR data and that of the probed subsurface high-frequency electromagnetic velocity field, the latter of which is strongly related to soil water content. Based on this relationship, we used a Monte-Carlo inversion strategy to estimate the correlation structure of the subsurface water content distribution from 3D GPR data acquired at a particularly well characterized test site. By inverting two collocated 3D GPR datasets collected at nominal source frequencies of 100 and 200 MHz, we obtain consistent information regarding the aspect ratios of the water content distribution, which are in agreement with independent and unrelated previous studies. In contrast to earlier related work, we also find that it is indeed possible to constrain the Hurst number, which is a key parameter characterizing the complexity of the fine-scale sedimentary structure.

As we consider data collected in the saturated zone, where water content is equivalent to porosity, our results can be directly compared to independent estimates of the correlation structure of porosity at the study site. Indeed, the detailed results of our work, notably the inferred spatial anisotropy and the spatial orientation of the corresponding principle axes x', y', and z', should allow for substantial refinements in the conditional stochastic simulations of the 3D porosity structure at the BHRS. This, turn, points to points to the immense potential of the proposed method in the context of detailed hydrogeophysical site characterizations.

The results of this study demonstrate that the proposed technique provides an effective means of inferring the second-order stochastic properties of the water content in the shallow subsurface based on surface-based GPR alone and without the need of borehole information for calibration purposes. This information is essential for the successful 3D geostatistical interpolation and/or stochastic simulation of sparse borehole measurements of related key hydraulic properties, such as the hydraulic conductivity.

Acknowledgements

This work was funded by a grant from the National Key R&D Program of China (Number 2017YFC0601504); a National Non-Profit Institute Research Grant from the Institute of Geophysical and Geochemical Exploration (Number WHS201309); the China National Natural Science Foundation (Number 41774145); and the China Scholarship Council (201706410035). We thank Jürg Hunziker for his help with setting up simulations on our institute computing cluster. We also thank Michael Knoll and Warren Barrash who collected the GPR data as part of the initial BHRS characterization.

References

Aki, K. and Chouet, B. 1975. Origin of coda waves: Source, attenuation, and scattering effects. Journal of Geophysical Research 80 (23), 3322–3342. https://doi.org/10.1029/JB080i023p03322.

Al Hagrey, S.A. and Müller, C. 2000. GPR study of pore water content and salinity in sand. Geophysical Prospecting 48 (1), 63–85. https://doi.org/10.1046/j.1365-2478.2000.00180.x.

Barrash, W. and Clemo, T. 2002. Hierarchical geostatistics and multifacies systems: Boise Hydrogeophysical Research Site, Boise, Idaho. Water Resources Research 38 (10), 14-1-14–18. https://doi.org/10.1029/2002WR001436.

Berkhout, A.J. 1984. Seismic resolution: A quantitative analysis of resolving power of acoustical echo techniques. Geophysical Press.

Beven, K. and Binley, A. 1992. The future of distributed models: Model calibration and uncertainty prediction. Hydrological Processes 6 (3), 279–298. https://doi.org/10.1002/hyp.3360060305.

Bradford, J.H., Clement, W.P. and Barrash, W. 2009. Estimating porosity with ground-penetrating radar reflection tomography: A controlled 3-D experiment at the Boise Hydrogeophysical Research Site. Water Resources Research 45 (4), 1–11. https://doi.org/10.1029/2008WR006960.

Cardiff, M., Bakhos, T., Kitanidis, P.K. and Barrash, W. 2013. Aquifer heterogeneity characterization with oscillatory pumping: Sensitivity analysis and imaging potential. Water Resources Research 49 (9), 5395–5410. https://doi.org/10.1002/wrcr.20356.

Dafflon, B. and Barrash, W. 2012. Three-dimensional stochastic estimation of porosity distribution: Benefits of using ground-penetrating radar velocity tomograms in simulated-annealing- based or Bayesian sequential simulation approaches. Water Resources Research 48 (5), 1–13. https://doi.org/10.1029/2011WR010916.

Dafflon, B., Irving, J. and Barrash, W. 2011. Inversion of multiple intersecting high-resolution crosshole GPR profiles for hydrological characterization at the Boise Hydrogeophysical Research Site. Journal of Applied Geophysics 73 (4), 305–314. https://doi.org/10.1016/j.jappgeo.2011.02.001.

Dafflon, B., Irving, J. and Holliger, K. 2009. Simulated-annealing-based conditional simulation for the local-scale characterization of heterogeneous aquifers. Journal of Applied Geophysics 68 (1), 60–70. https://doi.org/10.1016/j.jappgeo.2008.09.010.

Dafflon, B., Tronicke, J. and Holliger, K. 2005. Inferring the lateral subsurface correlation structure from georadar data: Methodological background and experimental evidence, in: Geostatistics for Environmental Applications. Springer, pp. 467–478, https://doi.org/10.1007/b137753.

Dolan, S. and Bean, C.J. 1997. Some remarks on the estimation of fractal scaling parameters from borehole wire-line logs. Geophysical Research Letters 24 (10),

1271–1274. https://doi.org/10.1029/97GL00987.
Ernst, J.R., Green, A.G., Maurer, H. and Holliger, K. 2007. Application of a new 2D time-domain full-waveform inversion scheme to crosshole radar data. Geophysics 72 (5), J53–J64. https://doi.org/10.1190/1.2761848.
Frankel, A. and Clayton, R.W. 1986. Finite difference simulations of seismic scattering: Implications for the propagation of short-period seismic waves in the crust and models of crustal heterogeneity. Journal of Geophysical Research 91 (B6), 6465. https://doi.org/10.1029/JB091iB06p06465.
Gibson, B. 1991. Analysis of lateral coherency in wide-angle seismic images of heterogeneous targets. Journal of Geophysical Research 96 (B6), 10261. https://doi.org/10.1029/91JB00340.
Gloaguen, E., Chouteau, M., Marcotte, D. and Chapuis, R. 2001. Estimation of hydraulic conductivity of an unconfined aquifer using cokriging of GPR and hydrostratigraphic data. Journal of Applied Geophysics 47 (2), 135–152. https://doi.org/10.1016/S0926-9851(01)00057-X.
Goff, J.A. and Jordan, T.H. 1988. Stochastic modeling of seafloor morphology: Inversion of sea beam data for second-order statistics. Journal of Geophysical Research: Solid Earth 93 (B11), 13589–13608. https://doi.org/10.1029/JB093iB11p13589.
Greaves, R.J., Lesmes, D.P., Lee, J.M. and Toksöz, M.N. 1996. Velocity variations and water content estimated from multi- offset, ground- penetrating radar. Geophysics 61 (3), 683–695. https://doi.org/10.1190/1.1443996.
Hardy, H.H. and Beier, R.A. 1994. Fractals in reservoir engineering. World Scientific. https://doi.org/10.1142/2574.
Hartzell, S., Harmsen, S. and Frankel, A. 2010. Effects of 3D random correlated velocity perturbations on predicted ground motions. Bulletin of the Seismological Society of America 100 (4), 1415–1426. https://doi.org/10.1785/0120090060.
Hochstetler, D.L., Barrash, W., Leven, C., Cardiff, M., Chidichimo, F. and Kitanidis, P.K. 2016. Hydraulic Tomography: Continuity and Discontinuity of High-K and Low-K Zones. Groundwater 54 (2), 171–185. https://doi.org/10.1111/gwat.12344.
Holliger, K., 1996. Seismic velocity heterogeneity of the upper crystalline crust as derived from a variety of P-wave sonic logs. Geophysical Journal International 125, 813-829. https://doi.org/10.1111/j.1365-246X.1996.tb06025.x.
Holliger, K., Carbonell, R. and Levander, A.R. 1992. Sensitivity of the lateral correlation function in deep seismic reflection data. Geophysical Research Letters 19 (22), 2263–2266. https://doi.org/10.1029/92GL02615.
Hu, B.X., Meerschaert, M.M. and Barrash, W., Hyndman, D.W., He, C., Li, X. et. al. 2009. Examining the influence of heterogeneous porosity fields on conservative solute transport. Journal of Contaminant Hydrology 108 (3–4), 77–88. https://doi.org/10.1016/j.jconhyd.2009.06.001.
Hubbard, S. and Linde, N. 2010. Hydrogeophysics, in: Treatise on Water Science. pp. 401–434, Elsevier, Amsterdam.

Huisman, J.A., Hubbard, S.S., Redman, J.D. and Annan, A.P. 2003. Measuring soil water content with ground penetrating radar. Vadose Zone Journal 2 (4), 476. https://doi.org/10.2136/vzj2003.4760.

Irving, J. and Holliger, K. 2010. Geostatistical inversion of seismic and ground-penetrating radar reflection images: What can we actually resolve? Geophysical Research Letters 37 (21), 1–5. https://doi.org/10.1029/2010GL044852.

Irving, J., Knight, R. and Holliger, K. 2009. Estimation of the lateral correlation structure of subsurface water content from surface-based ground-penetrating radar reflection images. Water Resources Research 45 (12), 1–14. https://doi.org/10.1029/2008WR007471.

Irving, J., Scholer, M. and Holliger, K. 2010. Inversion for the stochastic structure of subsurface velocity heterogeneity from surface- based geophysical reflection images, in: Advances in Near- Surface Seismology and Ground- Penetrating Radar. Society of Exploration Geophysics. Tulsa, Oklahoma.

Jones, A.G. and Holliger, K. 1997. Spectral analyses of the KTB sonic and density logs using robust nonparametric methods. Journal of Geophysical Research: Solid Earth 102 (B8), 18391–18403. https://doi.org/10.1029/96JB03668.

Knight, R., Tercier, P. and Irving, J. 2004. The effect of vertical measurement resolution on the correlation structure of a ground penetrating radar reflection image. Geophysical Research Letters 31 (21), n/a-n/a. https://doi.org/10.1029/2004GL021112.

Knight, R., Irving, J., Tercier, P., Freeman, G.J., Murray, C.J. and Rockhold, M.L. 2007. A comparison of the use of radar images and neutron probe data to determine the horizontal correlation length of water content, in: Subsurface Hydrology Data Integration for Properties & Processes. pp. 31–44. https://doi.org/10.1029/171GM05.

Kobr, M., Mareš, S. and Paillet, F. 2005. Geophysical well logging, in: Hydrogeophysics. pp 291-331. Springer. https://doi.org/10.1007/1-4020-3102-5_10.

Kowalsky, M.B., Finsterle, S., Peterson, J., Hubbard, S., Rubin, Y., Majer, E. et al. 2005. Estimation of field-scale soil hydraulic and dielectric parameters through joint inversion of GPR and hydrological data. Water Resources Research 41 (11). https://doi.org/10.1029/2005WR004237.

Leven, C. and Dietrich, P. 2006. What information can we get from pumping tests? comparing pumping test configurations using sensitivity coefficients. Journal of Hydrology 319 (1–4), 199–215. https://doi.org/10.1016/j.jhydrol.2005.06.030.

Mas-Pla, J., Jim Yeh, T., McCarthy, J.F. and Williams, T.M. 1992. A forced gradient tracer experiment in a coastal sandy aquifer, Georgetown site, South Carolina. Ground Water 30 (6), 958–964. https://doi.org/10.1111/j.1745-6584.1992.tb01579.x.

Nichols, J., Mikesell, D. and Van Wijk, K. 2010. Application of the virtual refraction to near-surface characterization at the Boise Hydrogeophysical Research Site.

Geophysical Prospecting 58 (6), 1011–1021. https://doi.org/10.1111/j.1365-2478.2010.00881.x.

Oldenborger, G.A., Knoll, M.D. and Barrash, W. 2004. Effects of signal processing and antenna frequency on the geostatistical structure of ground-penetrating radar data. Journal of Environmental and Engineering Geophysics 9 (4), 201–212. https://doi.org/10.4133/JEEG9.4.201.

Phanikumar, M.S., Hyndman, D.W., Zhao, X. and Dybas, M.J. 2005. A three-dimensional model of microbial transport and biodegradation at the Schoolcraft, Michigan, site. Water Resources Research 41 (5). https://doi.org/10.1029/2004WR003376.

Pullammanappallil, S., Levander, A. and Larkin, S.P. 1997. Estimation of crustal stochastic parameters from seismic exploration data. Journal of Geophysical Research: Solid Earth 102 (B7), 15269–15286. https://doi.org/10.1029/97JB01144.

Radu, F.A., Suciu, N., Hoffmann, J., Vogel, A., Kolditz, O., Park, C. et al. 2011. Accuracy of numerical simulations of contaminant transport in heterogeneous aquifers : A comparative study. Advances in Water Resources 34 (1), 47–61. https://doi.org/10.1016/j.advwatres.2010.09.012.

Rea, J. and Knight, R. 1998. Geostatistical analysis of ground-penetrating radar data: A means of describing spatial variation in the subsurface. Water Resources Research 34 (3), 329–339. https://doi.org/10.1029/97WR03070.

Reboulet, E.C. and Barrash, W. 2003. Core, grain-size, and porosity data from the Boise Hydrogeophysical Research Site, Boise, Idaho. BSU CGISS Technical Report 03- 02.

Ritzi, R.W., Jayne, D.F., Zahradnik, A.J., Field, A.A. and Fogg, G.E. 1994. Geostatistical modeling of heterogeneity in glaciofluvial, buried-valley aquifers. Ground Water 32 (4), 666–674. https://doi.org/10.1111/j.1745-6584.1994.tb00903.x.

Roman, S., Axler, S., and Gehring, F.W. 2005. Advanced linear algebra. Springer. https://doi.org/10.1007/0-387-27474-X.

Rubin, Y. and Hubbard, S. 2006. Hydrogeophysics. Springer. https://doi.org/10.1007/1-4020-3102-5.

Salamon, P., Fernàndez-Garcia, D. and Gómez-Hernández, J.J. 2007. Modeling tracer transport at the MADE site: The importance of heterogeneity. Water Resources Research 43 (8). https://doi.org/10.1029/2006WR005522.

Sato, H. 1977. Energy propagation including scattering effects single isotropic scattering approximation. Journal of Physics of the Earth 25 (1), 27–41. https://doi.org/10.4294/jpe1952.25.27.

Scholer, M., Irving, J. and Holliger, K. 2010. Estimation of the correlation structure of crustal velocity heterogeneity from seismic reflection data. Geophysical Journal International 183 (3), 1408–1428. https://doi.org/10.1111/j.1365-246X.2010.04793.x.

Stolt, R.H. 1978. Migration by Fourier transform. Geophysics 43 (1), 23–48.

https://doi.org/10.1190/1.1440826.
Sudicky, E.A. 1986. A natural gradient experiment on solute transport in a sand aquifer: Spatial variability of hydraulic conductivity and its role in the dispersion process. Water Resources Research 22 (13), 2069–2082. https://doi.org/10.1029/WR022i013p02069.
Tronicke, J., Dietrich, P., Wahlig, U. and Appel, E. 2002. Integrating surface georadar and crosshole radar tomography: A validation experiment in braided stream deposits. Geophysics 67 (5), 1516–1523. https://doi.org/10.1190/1.1512747.
Tronicke, J., Holliger, K., Barrash, W. and Knoll, M.D., 2004. Multivariate analysis of cross-hole georadar velocity and attenuation tomograms for aquifer zonation. Water Resources Research 40 (1), 1–14. https://doi.org/10.1029/2003WR002031.
Van Overmeeren, R.A., Sariowan, S. V. and Gehrels, J.C. 1997. Ground penetrating radar for determining volumetric soil water content; results of comparative measurements at two test sites. Journal of Hydrology 197 (1–4), 316–338. https://doi.org/10.1016/S0022-1694(96)03244-1.

Tables

Table 1. Summary of the Monte-Carlo inversion results obtained for the two collocated 3D GPR data sets from the BHRS, based on 2000 output realizations. S.D. denotes the standard deviation.

Data	$a_{x'}/a_{z'}$		$a_{y'}/a_{z'}$		$a_{y'}/a_{x'}$		ν		
	Mean	S.D.	Mean	S.D.	Mean	S.D.	Mean	S.D.	Peak
100-MHz	6.25	0.90	13.11	1.70	2.13	0.37	0.15	0.04	0.12
200-MHz	5.67	1.34	10.23	2.56	1.83	0.34	0.25	0.09	0.18

Figures

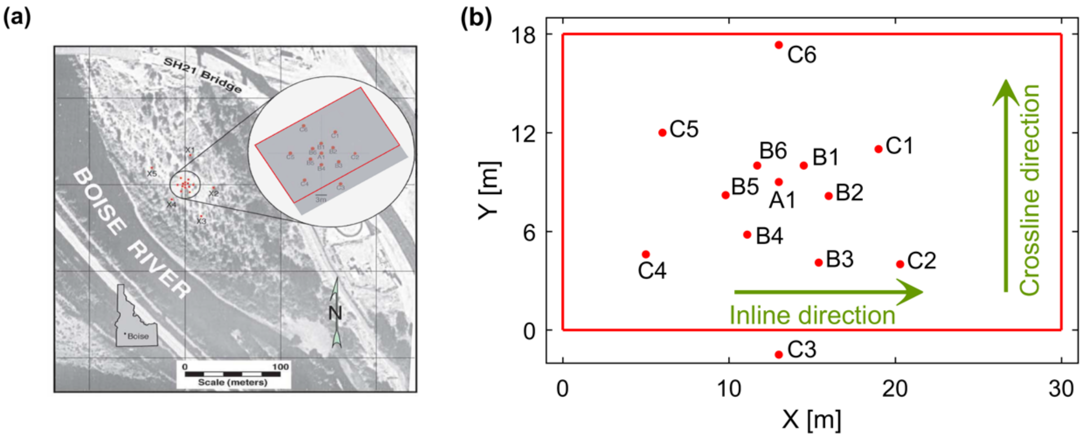

Figure 1: (a) Location of the BHRS with boreholes indicated by red dots and the position of the considered 3D GPR survey outlined in red. Modified after Bradford et al. (2009). (b) Zoomed-in view of the 3D GPR survey grid along with the well positions.

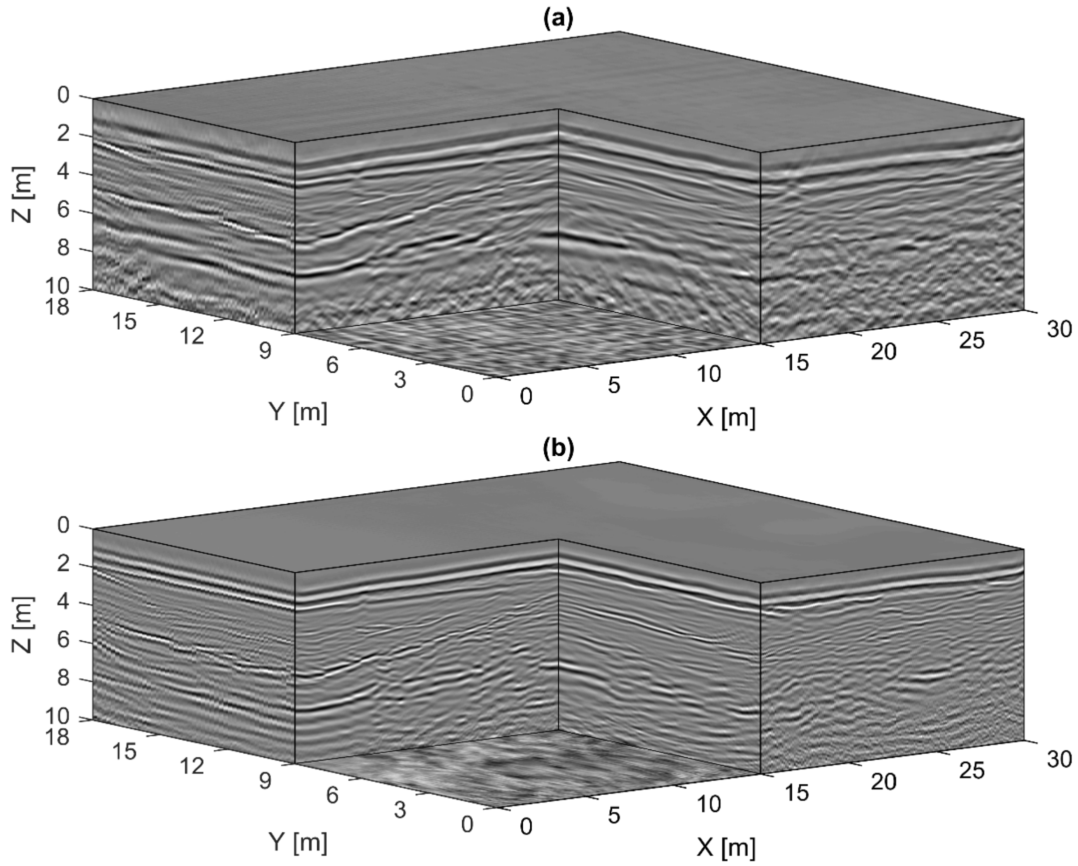

Figure 2: Processed and depth-migrated GPR data from the BHRS considered for analysis. The nominal antenna center frequency is (a) 100 MHz and (b) 200 MHz.

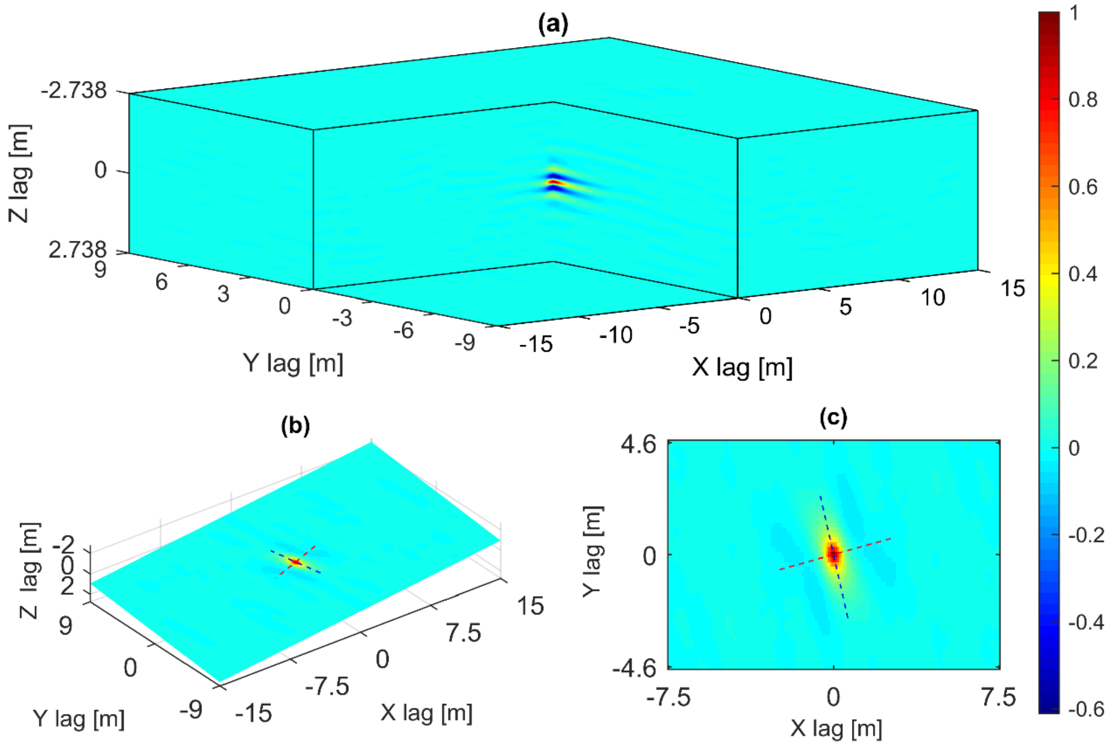

Figure 3: (a) 3D spatial autocorrelation of the 200-MHz GPR image from Figure 2b, calculated over a depth range of 2.5 m to 8 m, which corresponds to saturated sediments. (b) Slice through the autocorrelation in (a) along the predominant dipping plane of the sediments. (c) View of the slice in (b) from above. The red and blue dotted lines represent the x'- and y'-directions, respectively.

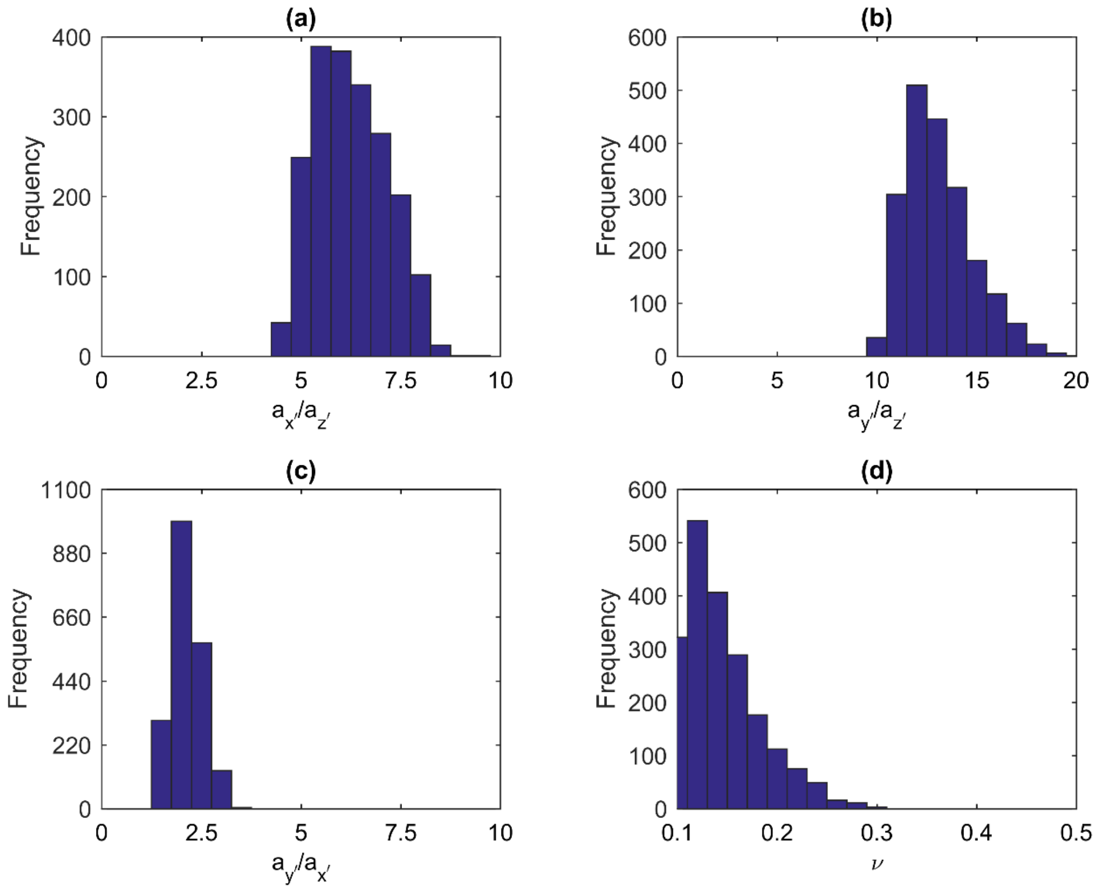

Figure 4: Histograms of Monte-Carlo inversion results obtained for the 100-MHz GPR data collected at the BHRS.

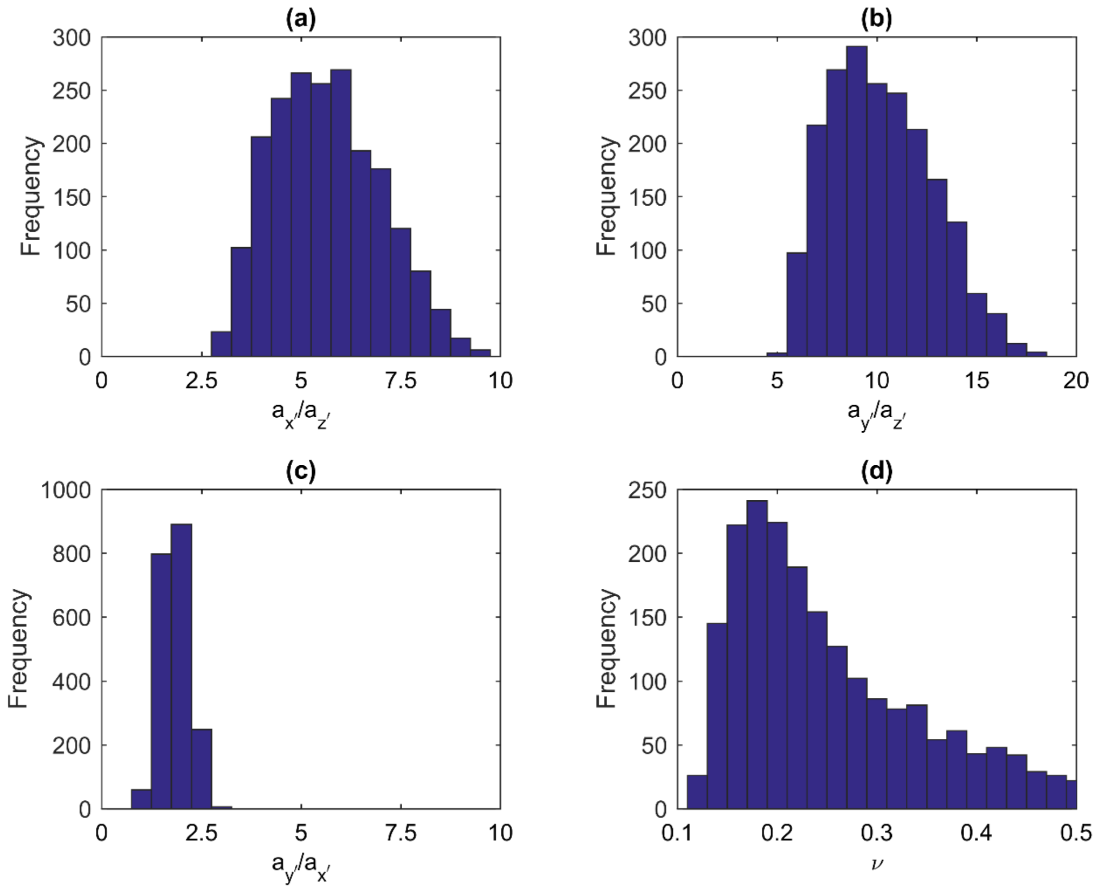

Figure 5: Histograms of Monte-Carlo inversion results obtained for the 200-MHz GPR data collected at the BHRS.